Micro-Optical Line Generator Metalens for a Visible Wavelength Based on Octagonal Nanopillars Made of Single-Crystalline Silicon

Satoshi Ikezawa, *Member, IEEE*, Ryota Yamada, Kosuke Takaki, Chikara Ogawa, and Kentaro Iwami, *Member, IEEE*

***Abstract*—Conventionally, silicon is less often selected as the material of dielectric metasurfaces in the visible band than other lossless materials, including titanium dioxide, silicon nitride, and gallium nitride. The reason is its relatively high extinction coefficient and resulting low transmittance. This study demonstrated that accurately designed nanopillars made of single-crystal silicon could be used satisfactorily on a metasurface, even in the visible band. Four line-focusing metasurface lenses were designed to verify the lens performance effectiveness of silicon nanopillars in the visible band. In addition, a combination of the character projection and the variable-shaped beam modes in the electron beam lithography was operated to evaluate the compatibility between mass productivity and accuracy. We successfully obtained a highly efficient line-focusing metasurface lens composed of single crystalline silicon nanopillars. The parameters of the metasurface lens at a wavelength of 532 nm were as follows: lens thickness, 300 nm; focal length, 3.91 mm; square aperture, 2 mm; numerical aperture, 0.25; measured transmittance, 38.4% to 46.8%; and measured beam spot width, 3.68 μm (full width at half maximum, FWHM) at the focal point. The results obtained in this study show a promising use of silicon metasurface for optical sensor applications in the visible band.**

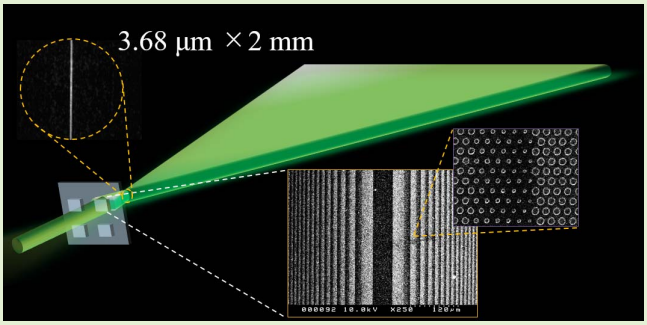

***Index Terms*—Dielectric metasurface, metasurface lens, metalens, single-crystal silicon, micro-optical line generator, planar optics.**

I. Introduction

METASURFACES have been successfully applied in several advanced micro-electro-mechanical systems (MEMS) sensors in the terahertz [1]–[11] and gigahertz [12]–[16] bands through both plasmonic and dielectric regimes. Owing to recent improvements in microfabrication technologies, metasurfaces have also been used in optical wavelengths [17]–[19] for various applications, including metasurface lenses (metalenses) [20]–[23], holography [24]–[29], waveplates [30]–[32], gratings [33]–[35], and functional optical devices [37]–[39].

Material selection is an essential aspect to consider in the design and fabrication of metasurfaces. For radio frequencies, metallic materials are preferred because of their ability to utilize plasmon resonance and high efficiency. However, dielectric materials have been attracting increasing attention at optical frequencies in recent years because of their lossless nature [40], [41], whereas the Ohmic loss has become a problem for metallic materials. This problem is crucial in the transmission mode.

Table I summarizes typically-used dielectric materials for metasurfaces at optical frequencies. Silicon is often used in infrared bands because of its high refractive index and low extinction coefficient. In the visible and ultraviolet regions, wide bandgap materials transparent in that wavelength range are often used. However, since a negative correlation generally exists between the bandgap and the refractive index, prioritizing transparency reduces the refractive index, posing fabrication challenges. In other words, to obtain a full 2π phase coverage, metasurfaces become thicker and require a

Manuscript received 6 May 2022; revised 13 June 2022; accepted 21 June 2022. Date of publication 30 June 2022; date of current version 1 August 2022. This work was supported in part by the Japan Society for the Promotion of Science (JSPS) KAKENHI under Grant 21H01781 and Grant 22K04894; in part by the Precise Measurement Technology Promotion Foundation; and in part by the Takeda Sentanchi Supercleanroom, University of Tokyo, through the "Nanotechnology Platform Program" of the Ministry of Education, Culture, Sports, Science, and Technology (MEXT), Japan, under Grant JPMXP09F11857. The associate editor coordinating the review of this article and approving it for publication was Dr. Rui Min. *(Corresponding author: Satoshi Ikezawa.)*

Satoshi Ikezawa, Ryota Yamada, Kosuke Takaki, and Kentaro Iwami are with the Department of Mechanical System Engineering, Tokyo University of Agriculture and Technology, Tokyo 184-8588, Japan (e-mail: s-ikezawa@go.tuat.ac.jp; k_iwami@cc.tuat.ac.jp).

Chikara Ogawa is with the Department of Industrial Technology and Innovation, Tokyo University of Agriculture and Technology, Tokyo 184-8588, Japan.

Digital Object Identifier 10.1109/JSEN.2022.3186060

TABLE I
OPERATING WAVELENGTHS AND MATERIALS FOR DIELECTRIC METASURFACES

Band	Wavelength [nm]	Materials
IR-C	≥3000	Si [42]
IR-B	1400–3000	Si [43], [45]–[47]
IR-A	780–1400	Si [48]–[52]
Visible	380–780	TiO_2 [53], [54], Si_3N_4 [55]–[57], GaN [58], [59], Glass [60], Diamond [61] Si [this work], [28], [36], [64]–[68]
UV	≤380	Nb_2O_5 [62], HfO_2 [63]

fabrication with a high aspect ratio. This makes the integration of MEMS sensors and metasurfaces difficult. Note that because single-crystal silicon (c-Si) is an indirect transition semiconductor, the extinction coefficient does not increase significantly even at wavelengths shorter than the bandgap, down to approximately 500 nm [28], [36]. Recent research found that metasurfaces made of c-Si exhibited sufficient transmittance in the visible range by optimizing their design dimensions [28], [36], [64]–[68]. Thus, the use of c-Si is considered a practical approach to developing functional sensors by integrating MEMS and metasurfaces due to the complementary metal-oxide-semiconductor (CMOS) compatibility. However, as detailed later, c-Si metasurfaces require precise dimensional control to prevent a decrease in transmittance due to unwanted modes. Typical point-beam type electron beam lithography (EBL) systems provide sufficient dimensional accuracy to accomplish this task, even though the processing throughput is low.

This study reports on the fabrication of c-Si metasurfaces using an electron beam lithography apparatus that involves a variable-shaped beam (VSB) mode and character projection (CP) mode to achieve high-speed e-beam writing for large area. In particular, a combination method of VSB and CP modes is proposed to achieve both fabrication compatibility and metalens functionality. As a demonstration, we adopt a line-focusing metalens that can be used for 3D scanning and analytical science. The design wavelength of 532 nm is chosen, which is one of the most widely used in laser excitation in Raman spectroscopy. A comparative verification of the proposed method is performed through the optical characterization of the fabricated line-focusing metalenses.

II. MATERIALS AND METHODS

The phase profile of a line-focusing lens $\phi(x)$ is given by the following equation:

$$\phi(x) = -\frac{2\pi}{\lambda}\left(\sqrt{f^2 + x^2} - f\right), \tag{1}$$

where λ is the wavelength, f is the focal length, and x is the position on the lens. Figure 1 shows the values of $\phi(x)$ for the parameters $\lambda = 532$ nm and $f = 3.91$ mm. The line-focusing metalens mimics this profile by arranging pillar-shaped waveguides by varying their dimension, showing the corresponding phase shift. The continuous occurrence of the phase shift can be controlled by changing the nanopillar width placed at x.

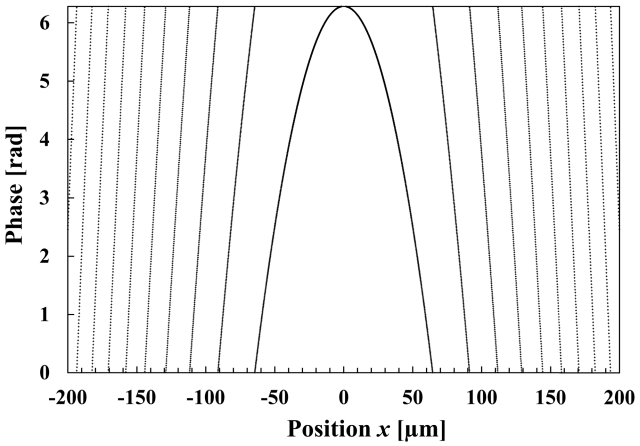

Fig. 1. Phase profile of the line generator lens. The vertical axis is folded back at a period of 2π.

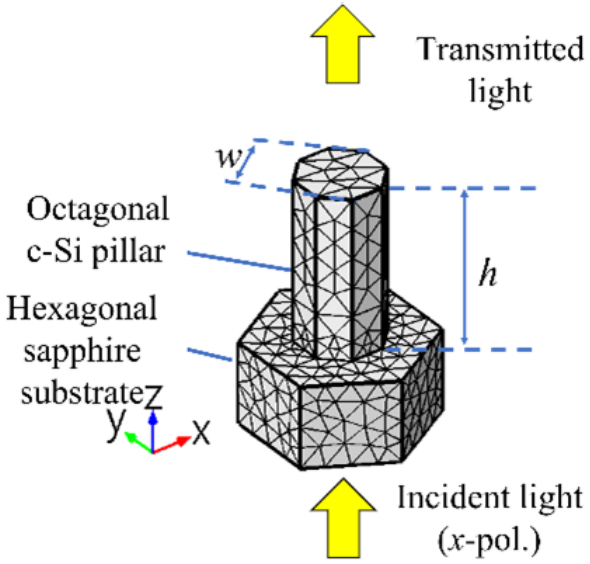

Fig. 2. Simulation setup for electromagnetic field analysis of the nanopillar.

A. Electromagnetic Field Analysis of Nanopillars

The electromagnetic field analysis of nanopillars was performed using a commercially available finite element method software (COMSOL Multiphysics 5.6, COMSOL Inc., USA) using the model illustrated in Figure 2. Materials of the nanopillar and the substrates were set as c-Si and sapphire, respectively, to represent a c-Si on sapphire (SOS) wafers. The octagonal cross-section was adopted to apply CP mode EBL, as detailed later. The hexagonal lattice is chosen to increase the fill factor to achieve a large phase shift. The period p of the lattice was fixed to 345 nm.

The electromagnetic wave frequency domain (ewfd) physics was considered in the calculations. The width w and height h of a nanopillar were used as parameters. The thickness of the sapphire substrate was $h/2$. The surrounding medium of the pillar was the air with a thickness of 1.5 h (not shown). The x-polarized light was incident from the bottom part of the sapphire substrate and emitted from the output

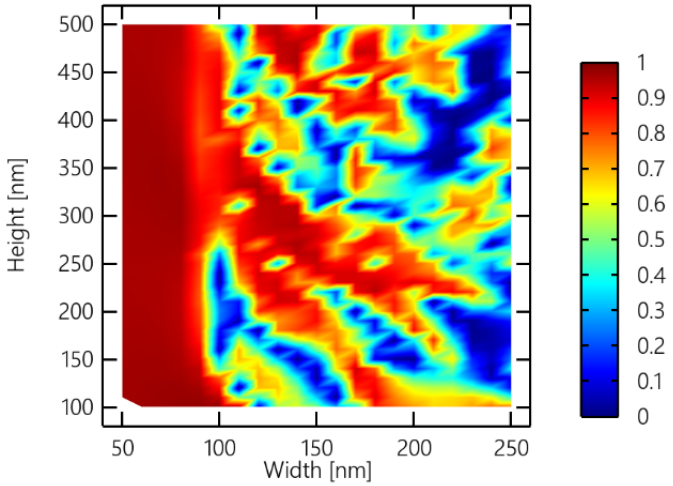

Fig. 3. Transmittance of c-Si nanopillar.

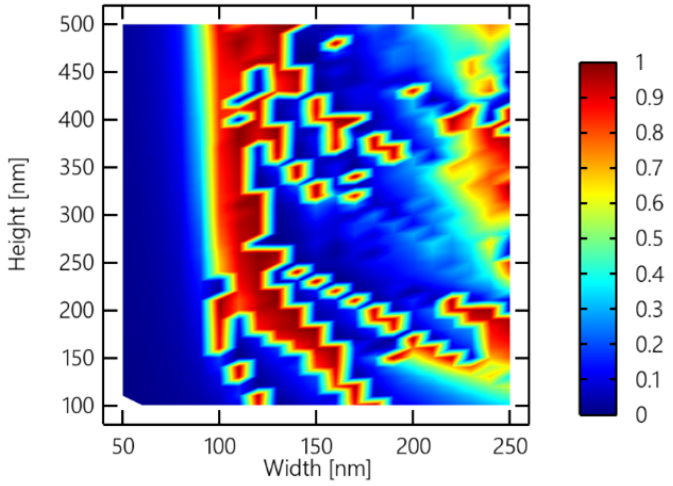

Fig. 4. Phase/2π of c-Si nanopillar.

port at the top of the surrounding air. The Floquet periodic boundary condition was applied to the remaining borders. The transmittance and the phase at the output port were monitored using the sweeping parameters w and h. Figures 3 and 4 show the parametric sweep results of the transmittance and phase/2π, respectively. Note that the nanopillar shows high transparency over a wide width range when the nanopillar height is approximately 300 nm.

Figure 5 shows the extracted transmittance and phase/2π at $h = 300$ nm with the width range from 90 to 280 nm and the step of 5 nm. As shown here, full 2π phase coverage can be achieved by using nanopillars with a width range from 90 to 280 nm. However, some pillars show low transmittance. In order to achieve high average transmittance, these pillars should be eliminated.

B. Selection of Nanopillars Based on the EBL Apparatus

The appropriate selection of nanopillars, considering the characteristics of the fabrication apparatus, is essential to achieve both sufficient transmittance and high throughput.

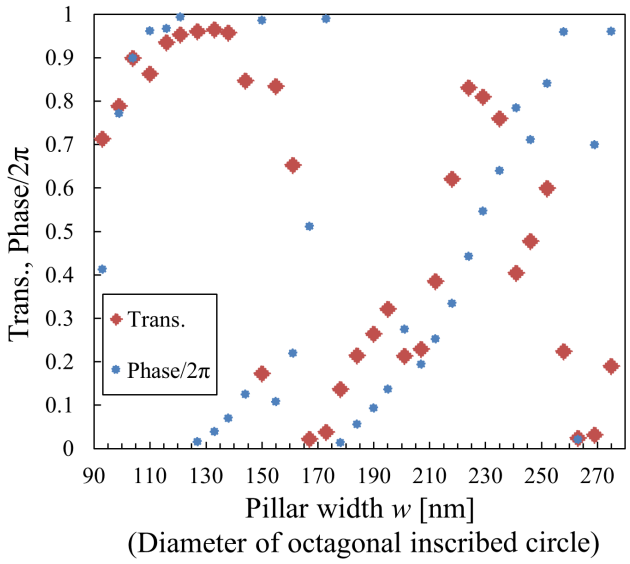

Fig. 5. Extracted plots of transmittance and phase/2π at $h = 300$ nm.

In this study, we used an EBL apparatus F7000S-VD02 (Advantest, Japan) that supports both CP and VSB modes. In particular, the CP mode uses dedicated stencils to shape electron beams to write pre-registered features with superior throughput. The VSB mode expresses any feature with the combination of rectangles, even though the writing speed decreases [69]–[71]. As the apparatus has octagonal CPs with the width-across-flat from 50 to 300 nm with a 10 nm step, intermediate sizes must be written using VSB mode.

We decided to use CP as much as possible while using VSB to assist where the phase leaps were substantial to achieve high throughput while avoiding low transmittance pillars. Figure 6 shows the phasor diagram of the selected pillars to assess the average transmittance and the continuity of the phase steps. [72]. This selection hereafter is referred to as non-correction (NC). For the inner orange plot, the radius and argument show a transmittance T_i and phase ϕ_i. The outer plot is a projection of the unit circle. The CP and VSB notations in the figure indicate the EBL mode and designed size combination, which are used as cell names on the CAD layout file.

C. Selection of Nanopillars Considering Fabrication Errors

Error correction between the nominal (designed) size and the actual (fabricated) size of the selected nanopillars was conducted. The sizes of the fabricated pillars were measured using scanning electron microscopy (SEM). Figure 7 shows the relationship between the nominal width w_i and the measured width w_o. We obtained the linear calibration line using the following equation:

$$w_o = a w_i + c, \tag{2}$$

where a and c are the correction coefficients, which are set to $a = 1.1362$ and $c = 24.811$ nm. The combined use of the CP and VSB modes show good linearity.

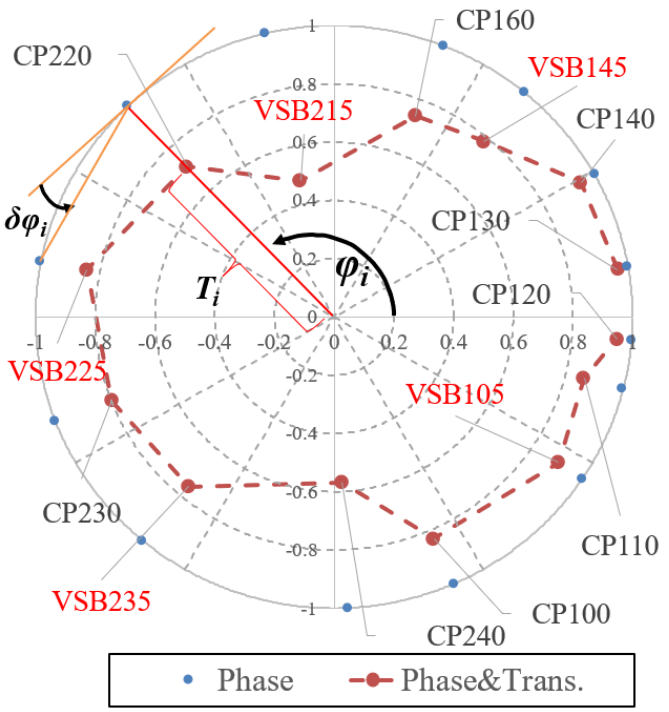

Fig. 6. Phasor diagram for selected nanopillars with the nominal widths of the CP and VSB methods.

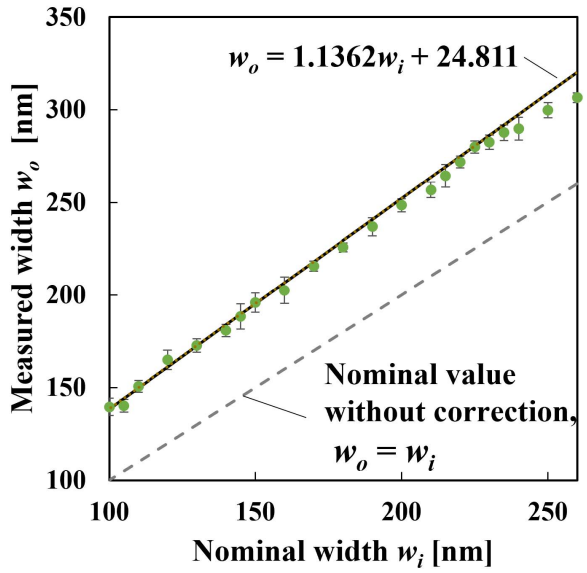

Fig. 7. Relationship between the design and measured widths of c-Si nanopillars with the calibration line for error compensation.

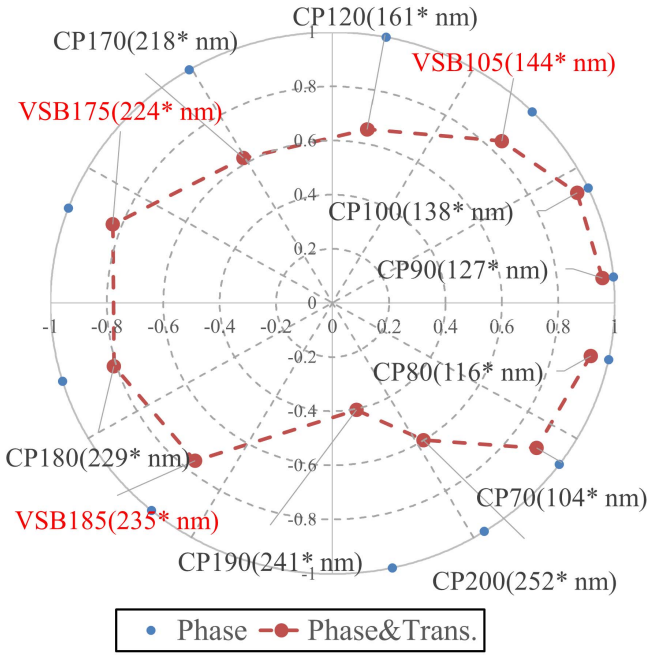

Fig. 8. Phasor diagram for selected nanopillars by considering the fabrication error.

TABLE II
LIST OF THE SELECTED NANOPILLARS

Cell name	w_o [nm]	I. CP_NC	II. CPVSB_NC	III. CP_C	IV. CPVSB_C
CP70	104	–	–	✓	✓
CP80	116	–	–	✓	✓
CP90	127	–	–	✓	✓
CP100	138	✓	✓	✓	✓
VSB105	144	–	✓	–	✓
CP110	150	✓	✓	–	–
CP120	161	✓	✓	✓	✓
CP130	173	✓	✓	–	–
CP140	184	✓	✓	–	–
VSB145	190	–	✓	–	–
CP160	207	✓	✓	–	–
CP170	218	–	–	✓	✓
VSB175	224	–	–	–	✓
CP180	229	–	–	✓	✓
VSB185	235	–	–	–	✓
CP200	241	–	–	✓	✓
CP210	252	–	–	✓	✓
VSB215	269	–	✓	–	–
CP220	275	✓	✓	–	–
VSB225	280	–	✓	–	–
CP230	286	✓	✓	–	–
VSB235	292	–	✓	–	–
CP240	297	✓	✓	–	–

I. CP_NC: Only the CP mode was used without size correction. II. CP-VSB_NC: Combination with CP and VSB modes without size correction. III. CP_C: Only the CP mode with size correction. IV. CP-VSB_C: Combination with CP and VSB modes with size correction.

The calibration line can be used to reselect the pillars based on Figure 5. Moreover, the pillar can be presented in the phasor expression, as shown in Figure 8. This selection hereafter is referred to as correction (C). The CP and VSB notations are cell names in the CAD layout, and the value with an asterisk in parentheses is w_o. Table II presents a list of selected pillars. We tried four selections: CP only or CPVSB combination, with (C) or without (NC) correction. They are referred to as CP_NC, CPVSB_NC, CP_C, and CPVSB_C. Based on these nanopillar selections, the line-focusing metalens was designed to have an aperture size of 2 mm and a numerical aperture NA of 0.25, according to Equation (1). A Python library and the gdstk package were used to arrange the nanopillars and GDSII layout file production.

D. Focusing Simulation

A focusing simulation of the line-focusing metalens was performed. In this regard, a 3D model corresponding to a

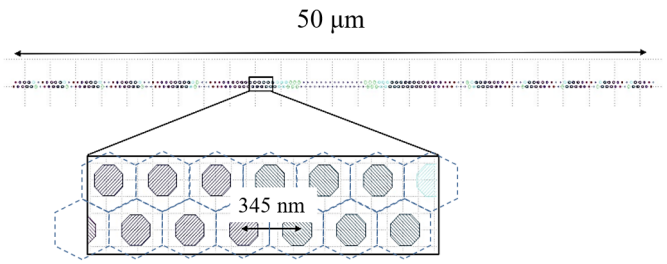

Fig. 9. CAD layout of the top view of the metasurface comprising an array of octagonal crystalline Si nanopillars arranged hexagonally with a lattice constant of $p = 345$ nm.

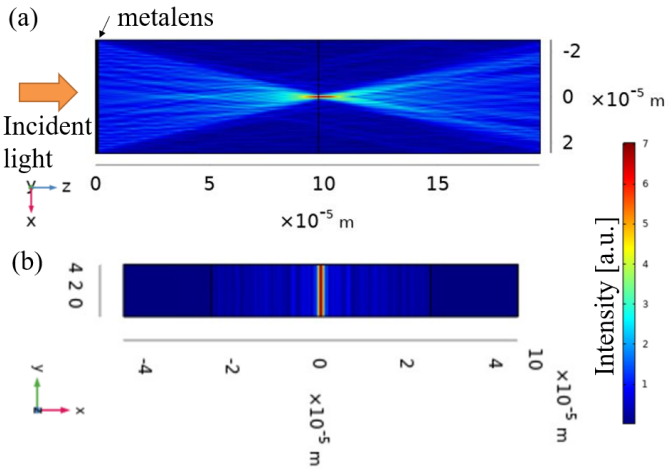

Fig. 10. Intensity distribution obtained using FEM simulation along the (a) $x - z$ plane and (b) $x - y$ plane at $z = f$.

one-period arrangement of the nanopillars was calculated using the electromagnetic wave, beam envelope (ewbe) physics of COMSOL. For the simulation, the aperture size d of the model was scaled down to 50 μm (1/40 of the design) while maintaining the numerical aperture of 0.25 and nanopillar dimensions to reduce the memory requirement. As shown in Figure 9, the one period of the hexagonal lattice was extracted along the x-axis, and the periodic boundary condition was applied for the y-boundary. The simulation was developed using the GDSII layout file obtained with the CPVSB_NC selection using the proper file conversion into COMSOL simulation. The degree of freedom of the model was approximately 20 million, and the model was solved using TSUBAME3.0 supercomputer at the Tokyo Institute of Technology. Figure 10 shows the calculated intensity distributions along the $x - z$ plane (a) and $x - y$ plane at the focal length $z = f$ (b). The metalens was placed at $z = 0$. The position of the beam waist agrees well with the theoretical focal length of $f = 95$ μm. Note that the Figure 10 is expanded 20 times in the y-direction due to its very thin size ($\sqrt{3}p = 598$ nm). The simulation results successfully confirmed the line focusing at the focal point.

III. Fabrication

A. Comparison of the EBL Writing Speed

The total number of pillars used in this study, i.e., 38,805,118, the fastest limit is 825.2 seconds in the point beam (PB) method (1nA condition) to write the pattern, 175.8 seconds in the CP mode, and 326.7 seconds in the CP-VSB combination mode. The octagonal shape in the CP mode has the most abundant size variation among the other polygon or circular shapes in this EBL apparatus. This study reports comparative optical verification results of the effectiveness of the line-focusing metalenses using the microscopic optical experimental setup.

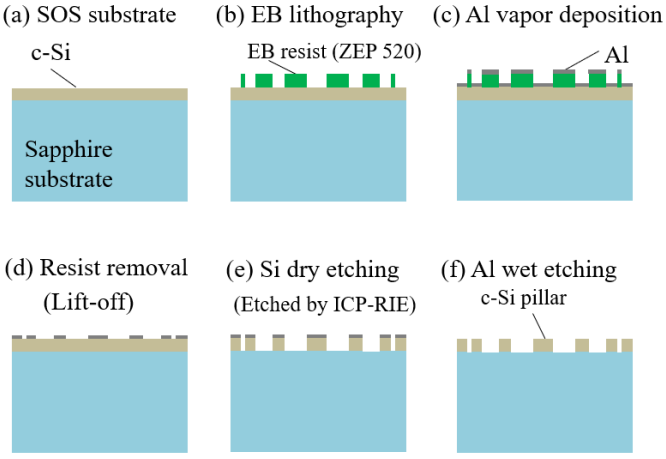

Fig. 11. Schematic of the fabrication process.

B. Fabrication Process

A schematic of the fabrication process is shown in Figure 11. A commercially-available SOS substrate (c-Si layer: 300 nm, sapphire substrate: 460 μm) was diced into 2 cm^2 chips (a). After cleaning, a positive electron beam (EB) resist (ZEP520A-7, ZEON, Japan) was spin-coated with a hexamethyldisilazane (HMDS) primer and an antistatic agent (ESPACER 300Z, Showa Denko, Japan).

Metalens patterns with four selections were written using the EBL apparatus with a dose of 104 μC/cm^2. After removing ESPACER, the resist pattern was developed (ZED-N50, Zeon, Japan) (b). Subsequently, after removing the resist residual by the O_2 plasma asher, the thin Al film was coated with vacuum evaporation (c). The EB resist was removed using the organic solvent dimethylacetamide (DMAC) (d). The Si layer of the substrate was etched using an inductively-coupled plasma reactive ion etching (ICP-RIE) apparatus (NE-550, ULVAC, Japan) using Al masks. Finally, the Al mask was removed using an etchant solution.

Figure 12 presents the SEM images of the fabricated metalens (CPVSB_C). The figure shows the periodic structure of the central part of the 2-mm-wide metalens. The inset image depicts the boundary region between the smallest (104 nm) and the widest (252 nm) pillars. As shown in the SEM images, the selected pillars were successfully fabricated among all ranges of selected widths.

IV. Characterization of the Fabricated Metalenses

A. Demonstration of Line Focusing and Laser Line Generation

Figure 13 demonstrates the line focusing by the metalenses with four selections obtained using a room light. Note that

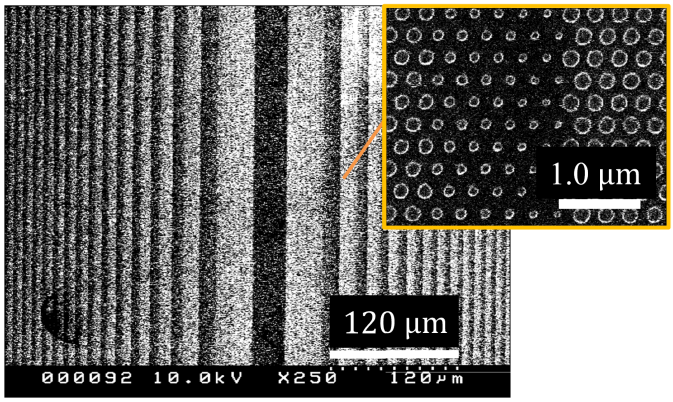

Fig. 12. SEM images of the fabricated metalens (CPVSB_C).

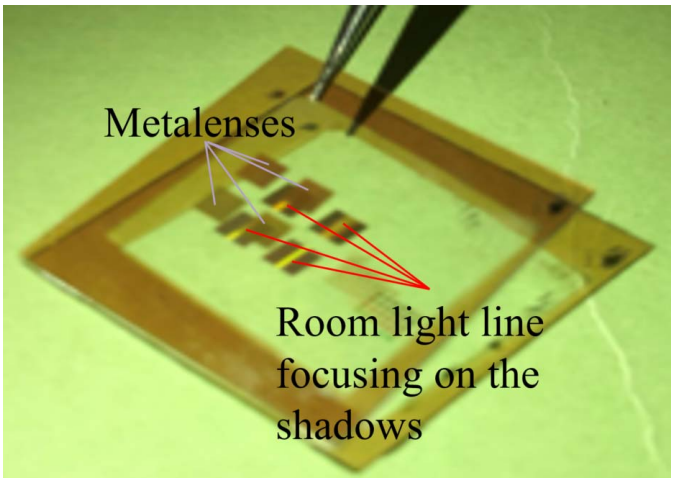

Fig. 13. Demonstration of line focusing by the fabricated metalenses under room right.

all four metalenses successfully show lines focusing on their shadows. These four metalenses correspond to those listed in Table II. Figure 14 shows the wide projection angle line generation in the far field by emitting a laser with a wavelength of 532 nm into the line focusing metalens. The laser beam spreads horizontally with a wide divergence angle after passing through the focal point, and the laser line in the far field is successfully generated.

Transmittances of metalenses to the sapphire substrate reference are summarized in Table III measured using a photodiode power sensor (S120C, Thorlabs Inc., USA). All four metalenses achieved a transmittance of approximately 40%; therefore, the Si metasurface has sufficient transmittance for practical use in the visible band. Although the above results of transmission efficiency are not as good as those of previous study [67], the presented fabrication method ensure practical transmittance and has advantages in high speed e-beam writing for large area. From the results of these four transmittance observations, the set with size correction (III and IV) was found to have better transmittance characteristics than the set without size correction (I and II). Further, the set (I and III) using only the CP mode exhibited better transmittance characteristics than the CP-VSB combination (II and IV) set.

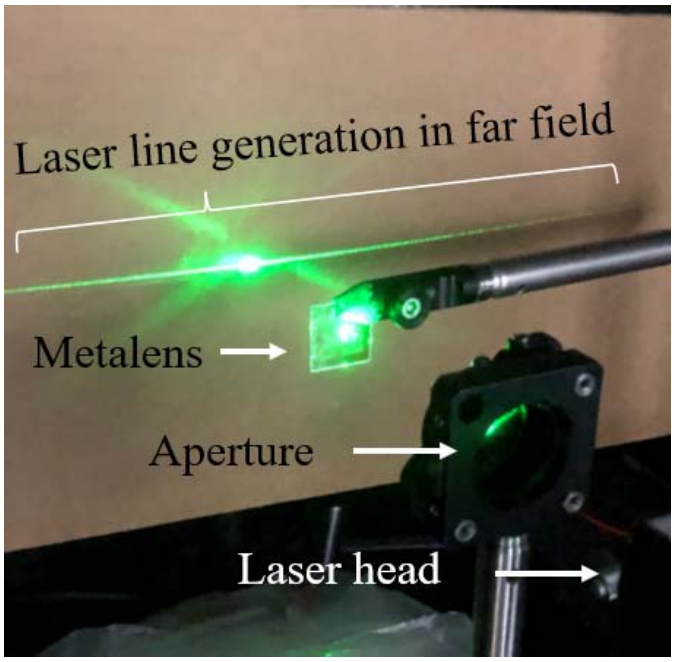

Fig. 14. Demonstration of the laser line generation in the far field.

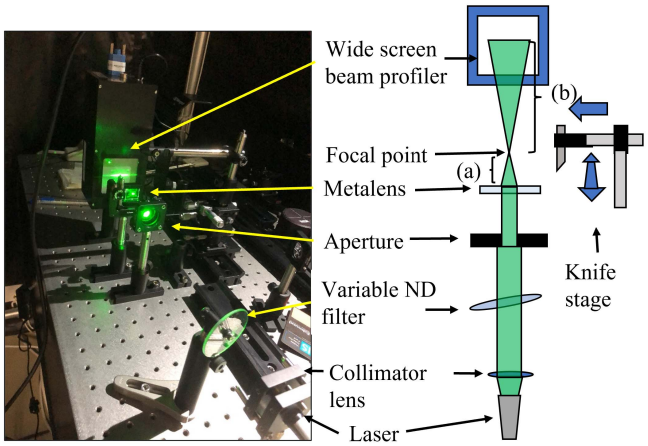

Fig. 15. Photograph and schematic of the experimental system for the knife-edge method.

B. Focal Distance Measurement by the Knife-Edge Method

The focal distance of the line-focusing metalens was evaluated following the knife-edge method using the experimental setup shown in Figure 15. We used a widescreen beam profiler (Lase View-LHB-mini, Kokyo, Inc.) to identify the beam shape hidden by the knife blade. The beam width was obtained from the knife blade displacement from a two-axis linear translation stage.

The result of the metalens (IV. CPVSB_C) is shown in Figure 16. The focal length of $f = 3.91$ mm was observed, which agrees well with the design and corresponds to the numerical aperture of $NA = 0.25$. The measurements were conducted three times separately for measurement ranges of (1) $z = 0.9$ to 5.9 mm, (2) $z = 3.45$ to 4.20 mm, and

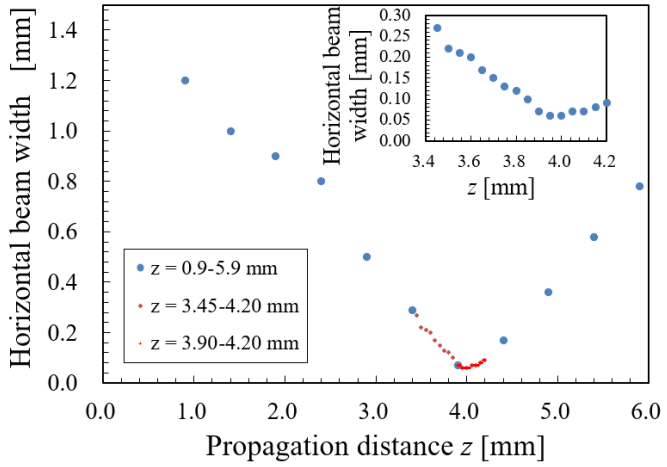

Fig. 16. Measured beam width with the distance range from 0.9 to 5.9 mm (main plot) and from 3.45 to 4.20 mm (inset).

TABLE III
TRANSMITTANCES OF THE METALENSES [%]

Selection	I. CP_NC	II. CPVSB_NC	III. CP_C	IV. CPVSB_C
Transmittance [%]	42.9	38.4	46.8	41.9

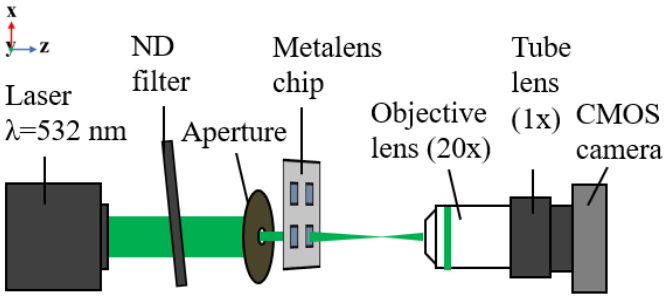

Fig. 17. Setup schematic for focal spot observation.

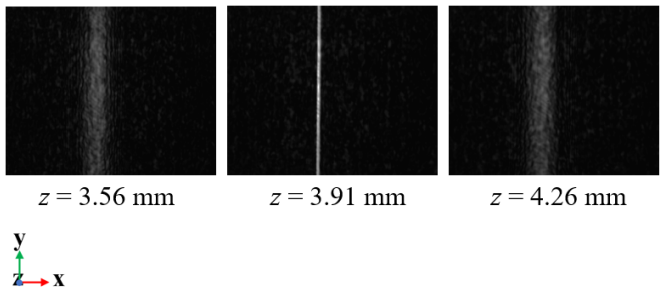

Fig. 18. Micro-tomographic pictures of a line-converged beam near the focal point and optically reconstructed propagation image.

(3) $z = 3.90$ to 4.20 mm. Almost identical focal lengths were obtained for other metalenses (I. CP_NC, II. CP-VSB_NC, and III. CP_C).

C. Evaluation of Focusing Performance

The focusing behavior of the fabricated metalenses at the design wavelength of 532 nm was evaluated with the setup shown in Figure 17. A laser ($\lambda = 532$ nm) was used with a neutral density filter and an aperture (ID25M, Thorlabs Inc., USA) with a diameter of 1 mm. A line-focusing metalens chip was mounted on a manual two-axis stage. The focal spot images were captured by using a monochrome complementary CMOS camera (DCC1545M, Thorlabs Inc., USA) with a 20× objective lens (M-PLAN APO 20× $NA = 0.42$, Mitutoyo, Japan) and a 1× tube lens (MT-40, Mitutoyo, Japan).

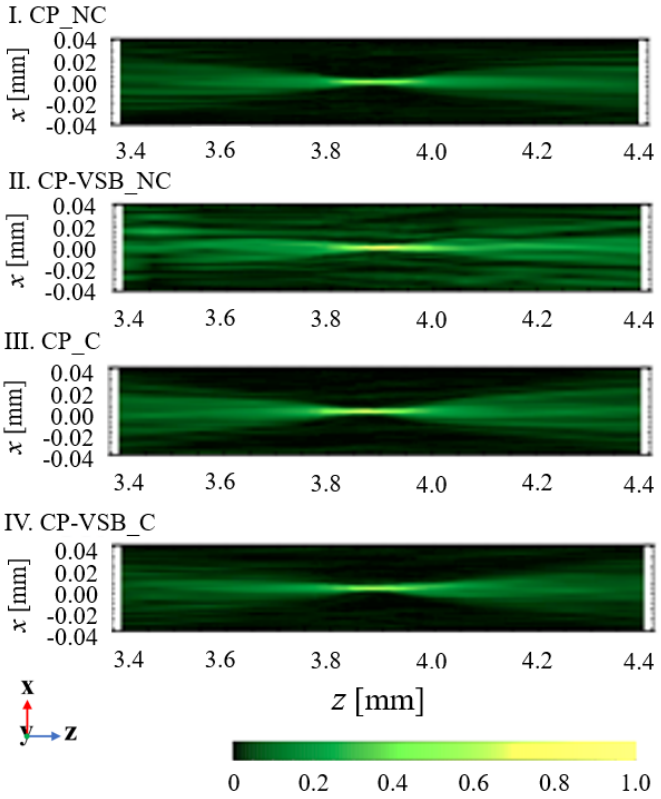

Fig. 19. Reconstructed intensity distributions in $x - z$ plane.

Figure 18 shows the captured images from the metalens (IV. CPVSB_C) at the distances of $z = 3.56$, 3.91, and 4.26 mm. The tightest focusing was obtained at the designed focal length of $z = 3.91$ mm.

Figure 19 shows tomographic reconstruction images of each metalens. These images were reconstructed from 37 pictures with a 0.1 mm increment along the $z-$axis for each lens, as shown in Figure 18. The x coordinates were calculated from the size of the image sensor and the magnification of the objective lens.

The color bar indicates the relative intensity of the obtained signal.

Figure 20 depicts the intensity distributions at the focal point extracted from Figure 18. The peak intensities and line widths (FWHM) are summarized in Table IV. The III. CP_C metalens exhibited the highest intensity and narrowest FWHM. Moreover, IV. CPVSB_C shows tight focusing as III. CP_C, even though a slight decrease in the peak intensity was present.

D. Modulation Transfer Function (MTF) Analysis

The focusing performances of four metalenses shown in Figure 20 were analyzed using the modulation transfer function (MTF).

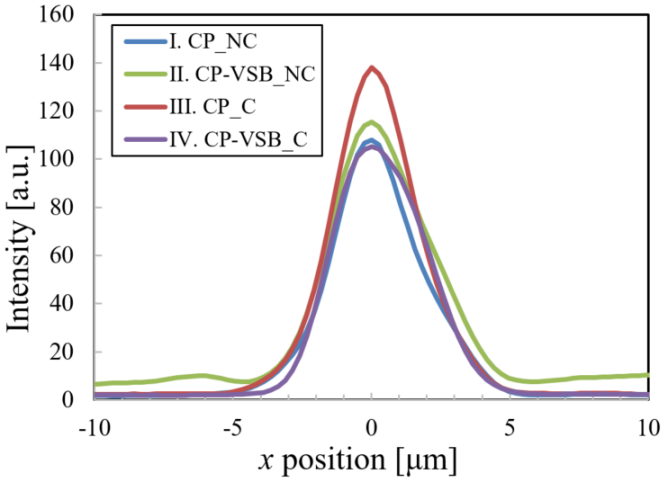

Fig. 20. Comparison of the intensity and full width at half maximum (FWHM) at the focal positions of four metalenses.

TABLE IV
PEAK INTENSITY AND FOCUSING-LINE WIDTH

	I. CP_NC	II. CPVSB_NC	III. CP_C	IV. CPVSB_C
Peak intensity [a.u.]	107.8	115.4	138.0	105.1
Line width (FWHM) [μm]	3.90	4.44	3.69	3.68

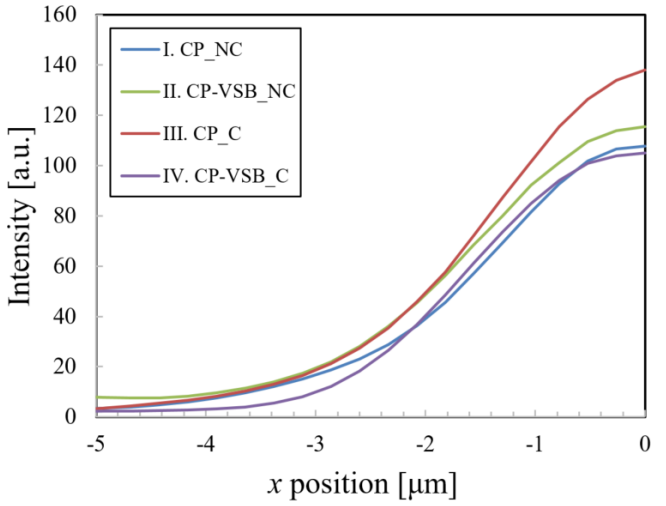

Fig. 21. Edge spread function for four metalenses.

Figure 21 shows the edge spread functions (ESF) of metalenses cropped from Figure 20. These ESFs were converted to the line spread functions (LSF), as shown in Figure 22. Subsequently, MTFs were obtained through the Fourier transform of the normalized LSFs, as shown in Figure 23. The black dashed line indicates the diffraction limit. Each dashed line corresponds to an approximate curve based on a moving average between two points. From this result, the IV. CPVSB_C metalens exhibited the best performance, even though the differences within the comparison range are not substantial.

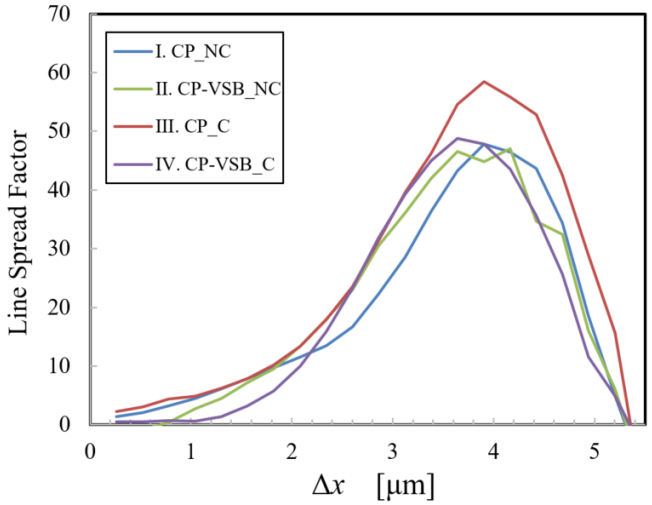

Fig. 22. Line spread function for four metalenses.

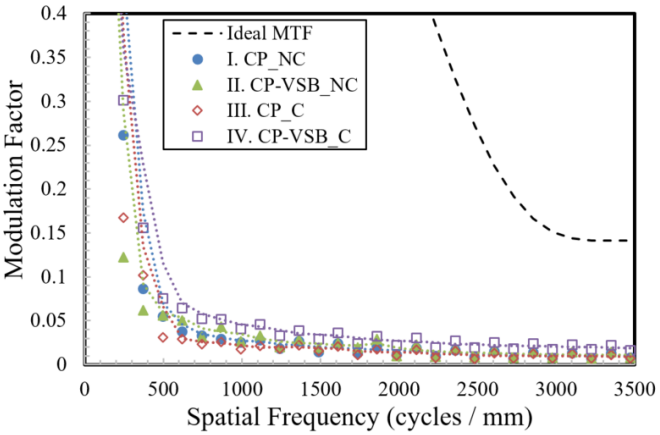

Fig. 23. Modulation transfer functions (MTFs) of the fabricated metalenses. The black dashed line represents the diffraction limit.

This result is in agreement with the FWHM performance listed in Table IV.

V. DISCUSSION

The results showed that a line generator Si metalens operating at a visible wavelength region could be used with sufficient transparency. We mainly adopted the CP mode as an EBL writing method suitable for a high production throughput, which is helpful for installing on a sensor device. Simultaneously, the VSB mode complemented the CP mode. A comparison of the exposure times indicated that the CP writing pattern was the fastest, followed by the CP-VSB combination mode. The VSB mode had a low manufacturing speed; however, both the CP mode and VSB mode were faster than the typical point beam exposure method in EBL.

Regarding the manufacturing quality, based on the experimental results of the line-focusing performance and MTF analysis, the CP-VSB combination mode was more effective in improving the optical performance of the metalens. Furthermore, based on the comparison results of the line-focusing performance and MTF analysis, the lens function of the metalenses with the size correction was confirmed to be superior

to the metalenses without size correction. This study shows that precise design with dimensional correction is essential for materials such as Si, where the phase shift is sensitively dependent on the nanopillar size. These results indicate that only size correction is not sufficient, and the synergistic effect of 5 nm structural complementation and manufacturing error correction ensures the optical function of the Si metasurface. As the pillar width accuracy should be less than 10 nm for producing the metalenses with various sizes in the visible wavelength, alternative materials with less phase shift fracturing and fabrication tolerance robustness are preferable. However, as demonstrated in this study, if the manufacturing accuracy is sufficient, more opportunities will arise for using Si metasurfaces with micro-optical sensor devices consisting of Si, which is the same material as the metasurface. Because Si has a high refractive index, it allows obtaining a much thinner structure to have sufficient phase shift than other materials. Moreover, Si metasurface might apply to MEMS sensors in a visible band by positively using them as micro-optical devices.

The proposed metalens can be both used in far fields and in near fields. For line-scan optics applications, it is applied from a few centimeters to a few meters. It also used for guiding light to the tight region, for example, the slit of a monochromator. The small and multifunctional technology of optical elements in the visible light region of Si material provides numerous opportunities for small cameras in mobile phones and wearable devices. For example, the high-precision metasurface fabrication method proposed in this study allows the development of miniature augmented reality (AR) devices, such as salt-grain-sized cameras, to be combined with compound-eye glasses and meta-optics.

Acknowledgment

The authors would like to thank Prof. Y. Mita, Dr. A. Higo, Dr. E. Lebrasseur, and M. Fujiwara (The University of Tokyo) for their support during sample fabrication, also would like to thank Prof. Lucas Heitzmann Gabrielli (University of Campinas) for developing and maintaining gdstk, a Python library for creating and manipulating GDSII layout files, and also would like to thank Editage (www.editage.com) for English language editing. Part of the numerical calculations was performed on a TSUBAME3.0 supercomputer at the Tokyo Institute of Technology.

References

[1] L. Jianchun, G. Pengwei, C. Bei, X. Wen, X. Xiaobo, and Y. Chuntao, "A terahertz microfluidic sensor based on metasurface," in *Proc. IEEE Asia–Pacific Microw. Conf. (APMC)*, Dec. 2019, pp. 1610–1612, doi: 10.1109/APMC46564.2019.9038226.

[2] Y. Ji, F. Fan, X. Zhang, J. Cheng, and S. Chang, "Active terahertz anisotropy and dispersion engineering based on dual-frequency liquid crystal and dielectric metasurface," *J. Lightw. Technol.*, vol. 38, no. 15, pp. 4030–4036, Aug. 1, 2020, doi: 10.1109/JLT.2020.2985667.

[3] Y. Zhong, L. Du, Q. Liu, L. Zhu, Y. Zou, and B. Zhang, "All-silicon terahertz metasurface with sharp Fano resonance and its sensing applications," *IEEE Photon. J.*, vol. 13, no. 2, pp. 1–10, Apr. 2021, doi: 10.1109/JPHOT.2021.3065096.

[4] A. Hamouleh-Alipour, A. Mir, and A. Farmani, "Analytical modeling and design of a graphene metasurface sensor for thermo-optical detection of terahertz plasmons," *IEEE Sensors J.*, vol. 21, no. 4, pp. 4525–4532, Feb. 2021, doi: 10.1109/JSEN.2020.3035577.

[5] X. Zhang, Y. Wang, X. Zhang, T. Zhou, K. Zhang, and X. Wang, "Carbon nanotubes film integrated with silicon microfluidic channel for a novel composite THz metasurface," *IEEE J. Sel. Topics Quantum Electron.*, vol. 28, no. 3, pp. 1–8, May 2022, doi: 10.1109/JSTQE.2021.3116969.

[6] A. Hamouleh-Alipour, A. Mir, and A. Farmani, "Design and analytical evaluation of a high resistance sensitivity bolometer sensor based on plasmonic metasurface structure," *IEEE J. Sel. Topics Quantum Electron.*, vol. 28, no. 2, pp. 1–7, Mar. 2022, doi: 10.1109/JSTQE.2021.3123049.

[7] T. Zhao *et al.*, "High efficiency flexible control of wave beams based on addition and subtraction operations on all dielectric reflection metasurfaces," *IEEE Sensors J.*, vol. 22, no. 5, pp. 4057–4068, Mar. 2022, doi: 10.1109/JSEN.2022.3143863.

[8] X. Chen, W. Fan, X. Jiang, and H. Yan, "High-Q toroidal dipole metasurfaces driven by bound states in the continuum for ultrasensitive terahertz sensing," *J. Lightw. Technol.*, vol. 40, no. 7, pp. 2181–2190, Apr. 1, 2022, doi: 10.1109/JLT.2021.3132727.

[9] Y. Wang *et al.*, "Properties and sensing performance of all-dielectric metasurface THz absorbers," *IEEE Trans. THz Sci. Technol.*, vol. 10, no. 6, pp. 599–605, Nov. 2020, doi: 10.1109/TTHZ.2020.3010164.

[10] F. Chen, Y. Cheng, and H. Luo, "Temperature tunable narrow-band terahertz metasurface absorber based on InSb micro-cylinder arrays for enhanced sensing application," *IEEE Access*, vol. 8, pp. 82981–82988, 2020, doi: 10.1109/ACCESS.2020.2991331.

[11] D. Yan *et al.*, "Terahertz refractive index sensing based on gradient metasurface coupled confined spoof surface plasmon polaritons mode," *IEEE Sensors J.*, vol. 22, no. 1, pp. 324–329, Jan. 2022, doi: 10.1109/JSEN.2021.3130266.

[12] J. Han *et al.*, "Adaptively smart wireless power transfer using 2-bit programmable metasurface," *IEEE Trans. Ind. Electron.*, vol. 69, no. 8, pp. 8524–8534, Aug. 2022, doi: 10.1109/TIE.2021.3105988.

[13] F. Alsolamy and A. Grbic, "Modal network formulation for the analysis and design of mode-converting metasurfaces in cylindrical waveguides," *IEEE Trans. Antennas Propag.*, vol. 69, no. 8, pp. 4598–4611, Aug. 2021, doi: 10.1109/TAP.2020.3048590.

[14] S. Paul and M. J. Akhtar, "Novel metasurface lens-based RF sensor structure for SAR microwave imaging of layered media," *IEEE Sensors J.*, vol. 21, no. 16, pp. 17827–17837, Aug. 2021, doi: 10.1109/JSEN.2021.3084614.

[15] J. Y. Dai *et al.*, "Simultaneous *in situ* direction finding and field manipulation based on space-time-coding digital metasurface," *IEEE Trans. Antennas Propag.*, vol. 70, no. 6, pp. 4774–4783, Jun. 2022, doi: 10.1109/TAP.2022.3145445.

[16] M. Lin *et al.*, "Single sensor to estimate DOA with programmable metasurface," *IEEE Internet Things J.*, vol. 8, no. 12, pp. 10187–10197, Jun. 2021, doi: 10.1109/JIOT.2021.3051014.

[17] N. I. Zheludev and Y. S. Kivshar, "From metamaterials to metadevices," *Nature Mater.*, vol. 11, pp. 917–924, Nov. 2012, doi: 10.1038/nmat3431.

[18] N. Yu and F. Capasso, "Flat optics with designer metasurfaces," *Nature Mater.*, vol. 13, pp. 139–150, Feb. 2014, doi: 10.1038/nmat3839.

[19] S. B. Glybovski, S. A. Tretyakov, P. A. Belov, Y. S. Kivshar, and C. R. Simovski, "Metasurfaces: From microwaves to visible," *Phys. Rep.*, vol. 634, pp. 1–72, May 2016, doi: 10.1016/j.physrep.2016.04.004.

[20] M. Khorasaninejad, W. T. Chen, R. C. Devlin, J. Oh, A. Y. Zhu, and F. Capasso, "Metalenses at visible wavelengths: Diffraction-limited focusing and subwavelength resolution imaging," *Science*, vol. 352, no. 6290, pp. 1190–1194, Jun. 2016, doi: 10.1126/science.aaf6644.

[21] W. T. Chen *et al.*, "A broadband achromatic metalens for focusing and imaging in the visible," *Nature Nanotechnol.*, vol. 13, pp. 220–226, Mar. 2018, doi: 10.1038/s41565-017-0034-6.

[22] F. Aieta, M. A. Kats, P. Genevet, and F. Capasso, "Multiwavelength achromatic metasurfaces by dispersive phase compensation," *Science*, vol. 347, no. 6228, pp. 1342–1345, Mar. 2015, doi: 10.1126/science.aaa2494.

[23] A. Arbabi, E. Arbabi, S. M. Kamali, Y. Horie, S. Han, and A. Faraon, "Miniature optical planar camera based on a wide-angle metasurface doublet corrected for monochromatic aberrations," *Nature Commun.*, vol. 7, no. 1, p. 13682, Dec. 2016, doi: 10.1038/ncomms13682.

[24] G. Zheng, H. Mühlenbernd, M. Kenney, G. Li, T. Zentgraf, and S. Zhang, "Metasurface holograms reaching 80% efficiency," *Nature Nanotechnol.*, vol. 10, no. 4, pp. 308–312, Apr. 2015, doi: 10.1038/nnano.2015.2.

[25] L. Huang *et al.*, "Three-dimensional optical holography using a plasmonic metasurface," *Nature Commun.*, vol. 4, no. 1, p. 2808, Dec. 2013, doi: 10.1038/ncomms3808.

[26] R. Izumi, S. Ikezawa, and K. Iwami, "Metasurface holographic movie: A cinematographic approach," *Opt. Exp.*, vol. 28, no. 16, pp. 23761–23770, Aug. 2020, doi: 10.1364/OE.399369.

[27] K. Huang *et al.*, "Silicon multi-meta-holograms for the broadband visible light," *Laser Photon. Rev.*, vol. 10, no. 3, pp. 500–509, May 2016, doi: 10.1002/lpor.201500314.

[28] N. Yamada, H. Saito, S. Ikezawa, and K. Iwami, "Demonstration of a multicolor metasurface holographic movie based on a cinematographic approach," *Opt. Exp.*, vol. 30, no. 10, pp. 17591–17603, May 2022, doi: 10.1364/OE.457460.

[29] C. Shen, R. Xu, J. Sun, Z. Wang, and S. Wei, "Metasurface-based holographic display with all-dielectric meta-axilens," *IEEE Photon. J.*, vol. 13, no. 5, pp. 1–5, Oct. 2021, doi: 10.1109/JPHOT.2021.3107442.

[30] K. Iwami, M. Ishii, Y. Kuramochi, K. Ida, and N. Umeda, "Ultra-small radial polarizer array based on patterned plasmonic nanoslits," *Appl. Phys. Lett.*, vol. 101, no. 16, Oct. 2012, Art. no. 161119, doi: 10.1063/1.4761943.

[31] M. Ishii, K. Iwami, and N. Umeda, "An Au nanofin array for high efficiency plasmonic optical retarders at visible wavelengths," *Appl. Phys. Lett.*, vol. 106, no. 2, Jan. 2015, Art. no. 021115, doi: 10.1063/1.4905369.

[32] M. Ishii, K. Iwami, and N. Umeda, "Highly-efficient and angle-independent zero-order half waveplate at broad visible wavelength based on Au nanofin array embedded in dielectric," *Opt. Exp.*, vol. 24, no. 8, pp. 7966–7976, Apr. 2016, doi: 10.1364/OE.24.007966.

[33] T. Shimura, T. Kinoshita, Y. Koto, N. Umeda, and K. Iwami, "Birefringent reconfigurable metasurface at visible wavelengths by MEMS nanograting," *Appl. Phys. Lett.*, vol. 113, no. 17, Oct. 2018, Art. no. 171905, doi: 10.1063/1.5046976.

[34] Y. Ra'di, D. L. Sounas, and A. Alù, "Metagratings: Beyond the limits of graded metasurfaces for wave front control," *Phys. Rev. Lett.*, vol. 119, no. 6, Aug. 2017, Art. no. 067404, doi: 10.1103/PhysRevLett.119.067404.

[35] D. Lin, P. Fan, E. Hasman, and M. L. Brongersma, "Dielectric gradient metasurface optical elements," *Science*, vol. 345, no. 6194, pp. 298–302, Jul. 2014, doi: 10.1126/science.1253213.

[36] C. Ogawa, S. Nakamura, T. Aso, S. Ikezawa, and K. Iwami, "Rotational varifocal moiré metalens made of single-crystal silicon meta-atoms for visible wavelengths," *Nanophotonics*, vol. 11, no. 9, pp. 1941–1948, Jan. 2022, doi: 10.1515/nanoph-2021-0690.

[37] A. Ahmadivand, B. Gerislioglu, R. Ahuja, and Y. K. Mishra, "Toroidal metaphotonics and metadevices," *Laser Photon. Rev.*, vol. 14, no. 11, Nov. 2020, Art. no. 1900326, doi: 10.1002/lpor.201900326.

[38] B. Gerislioglu, G. Bakan, R. Ahuja, J. Adam, Y. K. Mishra, and A. Ahmadivand, "The role of $Ge_2Sb_2Te_5$ in enhancing the performance of functional plasmonic devices," *Mater. Today Phys.*, vol. 12, Mar. 2020, Art. no. 100178, doi: 10.1016/j.mtphys.2020.100178.

[39] E. Maguid, I. Yulevich, D. Veksler, V. Kleiner, M. L. Brongersma, and E. Hasman, "Photonic spin-controlled multifunctional shared-aperture antenna array," *Science*, vol. 352, no. 6290, pp. 1202–1206, Apr. 2016, doi: 10.1126/science.aaf3417.

[40] A. Arbabi, Y. Horie, M. Bagheri, and A. Faraon, "Dielectric metasurfaces for complete control of phase and polarization with subwavelength spatial resolution and high transmission," *Nature Nanotechnol.*, vol. 10, no. 11, pp. 937–943, Nov. 2015, doi: 10.1038/nnano.2015.186.

[41] L. Wang *et al.*, "Grayscale transparent metasurface holograms," *Optica*, vol. 3, no. 12, pp. 1504–1505, Dec. 2016, doi: 10.1364/OPTICA.3.001504.

[42] X. Shi *et al.*, "All-dielectric orthogonal doublet cylindrical metalens in long-wave infrared regions," *Opt. Exp.*, vol. 29, no. 3, pp. 3524–3532, Feb. 2021, doi: 10.1364/OE.414001.

[43] M. Khorasaninejad *et al.*, "Achromatic metasurface lens at telecommunication wavelengths," *Nano Lett.*, vol. 15, no. 8, pp. 5358–5362, Aug. 2015, doi: 10.1021/acs.nanolett.5b01727.

[44] K. E. Chong *et al.*, "Efficient polarization-insensitive complex wavefront control using Huygens' metasurfaces based on dielectric resonant meta-atoms," *ACS Photon.*, vol. 3, no. 4, pp. 514–519, Apr. 2016, doi: 10.1021/acsphotonics.5b00678.

[45] M. I. Shalaev, J. Sun, A. Tsukernik, A. Pandey, K. Nikolskiy, and N. M. Litchinitser, "High-efficiency all-dielectric metasurfaces for ultra-compact beam manipulation in transmission mode," *Nano Lett.*, vol. 15, no. 9, pp. 6261–6266, Sep. 2015, doi: 10.1021/acs.nanolett.5b02926.

[46] T. Zhao *et al.*, "Cross-polarization carpet cloaking based on polarization conversion metasurfaces," *IEEE Sensors J.*, vol. 22, no. 7, pp. 6509–6517, Apr. 2022, doi: 10.1109/JSEN.2022.3150388.

[47] D. C. Zografopoulos and V. Dmitriev, "Quasi-dark resonances in silicon metasurface for refractometric sensing and tunable notch filtering," *J. Lightw. Technol.*, vol. 39, no. 21, pp. 6985–6993, Nov. 1, 2021, doi: 10.1109/JLT.2021.3107953.

[48] K. Iwami, C. Ogawa, T. Nagase, and S. Ikezawa, "Demonstration of focal length tuning by rotational varifocal moiré metalens in an ir-A wavelength," *Opt. Exp.*, vol. 28, no. 24, pp. 35602–35614, Nov. 2020, doi: 10.1364/OE.411054.

[49] J. Cheng *et al.*, "Ultra-compact structured light projector with all-dielectric metalenses for 3D sensing," *AIP Adv.*, vol. 9, no. 10, Oct. 2019, Art. no. 105016, doi: 10.1063/1.5121348.

[50] M. Kenney *et al.*, "Large area metasurface lenses in the NIR region," *Proc. SPIE*, vol. 11057, pp. 56–66, Jun. 2019, doi: 10.1117/12.2527157.

[51] S. Vo *et al.*, "Sub-wavelength grating lenses with a twist," *IEEE Photon. Technol. Lett.*, vol. 26, no. 13, pp. 1375–1378, Jul. 1, 2014, doi: 10.1109/LPT.2014.2325947.

[52] J. Ha, A. Ndao, L. Hsu, J.-H. Park, and B. Kante, "Planar dielectric cylindrical lens at 800 nm and the role of fabrication imperfections," *Opt. Exp.*, vol. 26, no. 18, pp. 23178–23184, Sep. 2018, doi: 10.1364/OE.26.023178.

[53] W. T. Chen, A. Y. Zhu, J. Sisler, Z. Bharwani, and F. Capasso, "A broadband achromatic polarization-insensitive metalens consisting of anisotropic nanostructures," *Nature Commun.*, vol. 10, no. 1, pp. 1–7, Jan. 2019, doi: 10.1038/s41467-019-08305-y.

[54] B. Groever, W. T. Chen, and F. Capasso, "Meta-lens doublet in the visible region," *Nano Lett.*, vol. 17, no. 8, pp. 4902–4907, Aug. 2017, doi: 10.1021/acs.nanolett.7b01888.

[55] M. Jang *et al.*, "Wavefront shaping with disorder-engineered metasurfaces," *Nature Photon.*, vol. 12, pp. 84–90, Jan. 2018, doi: 10.1038/s41566-017-0078-z.

[56] J. Xu, M. Cua, E. H. Zhou, Y. Horie, A. Faraon, and C. Yang, "Wide-angular-range and high-resolution beam steering by a metasurface-coupled phased array," *Opt. Lett.*, vol. 43, no. 21, pp. 5255–5258, Nov. 2018, doi: 10.1364/OL.43.005255.

[57] S. Colburn *et al.*, "Broadband transparent and CMOS-compatible flat optics with silicon nitride metasurfaces," *Opt. Mater. Exp.*, vol. 8, no. 8, pp. 2330–2344, Aug. 2018, doi: 10.1364/OME.8.002330.

[58] M.-H. Chen, W.-N. Chou, V.-C. Su, C.-H. Kuan, and H. Y. Lin, "High-performance gallium nitride dielectric metalenses for imaging in the visible," *Sci. Rep.*, vol. 11, no. 1, p. 6500, Mar. 2021, doi: 10.1038/s41598-021-86057-w.

[59] G. Brière *et al.*, "An etching-free approach toward large-scale light-emitting metasurfaces," *Adv. Opt. Mater.*, vol. 7, no. 14, Apr. 2019, Art. no. 1801271, doi: 10.1002/adom.201801271.

[60] J.-S. Park *et al.*, "All-glass, large metalens at visible wavelength using deep-ultraviolet projection lithography," *Nano Lett.*, vol. 19, no. 12, pp. 8673–8682, Dec. 2019, doi: 10.1021/acs.nanolett.9b03333.

[61] T.-Y. Huang *et al.*, "A monolithic immersion metalens for imaging solid-state quantum emitters," *Nature Commun.*, vol. 10, no. 1, pp. 1–8, Jun. 2019, doi: 10.1038/s41467-019-10238-5.

[62] K. Huang *et al.*, "Ultraviolet metasurfaces of ≈80% efficiency with antiferromagnetic resonances for optical vectorial anti-counterfeiting," *Laser Photon. Rev.*, vol. 13, no. 5, May 2019, Art. no. 1800289, doi: 10.1002/lpor.201800289.

[63] C. Zhang *et al.*, "Low-loss metasurface optics down to the deep ultraviolet region," *Light, Sci. Appl.*, vol. 9, no. 1, pp. 1–10, Apr. 2020, doi: 10.1038/s41377-020-0287-y.

[64] Y. Cui *et al.*, "Reconfigurable continuous-zoom metalens in visible band," *Chin. Opt. Lett.*, vol. 17, no. 11, 2019, Art. no. 111603.

[65] A. M. Shaltout *et al.*, "Spatiotemporal light control with frequency-gradient metasurfaces," *Science*, vol. 365, no. 6451, pp. 374–377, Jul. 2019, doi: 10.1126/science.aax2357.

[66] D. Sell, J. Yang, S. Doshay, K. Zhang, and J. A. Fan, "Visible light metasurfaces based on single-crystal silicon," *ACS Photon.*, vol. 3, no. 10, pp. 1919–1925, Oct. 2016, doi: 10.1021/acsphotonics.6b00436.

[67] Z. Zhou *et al.*, "Efficient silicon metasurfaces for visible light," *ACS Photon.*, vol. 4, no. 3, pp. 544–551, Mar. 2017, doi: 10.1021/acsphotonics.6b00740.

[68] H. Liang *et al.*, "Ultrahigh numerical aperture metalens at visible wavelengths," *Nano Lett.*, vol. 18, no. 7, pp. 4460–4466, Jul. 2018, doi: 10.1021/acs.nanolett.8b01570.

[69] E. Platzgummer, C. Klein, and H. Loeschner, "Electron multibeam technology for mask and wafer writing at 0.1 nm address grid," *J. Micro/Nanolithogr., MEMS, MOEMS*, vol. 12, no. 3, Aug. 2013, Art. no. 031108, doi: 10.1117/1.JMM.12.3.031108.

[70] A. Higo *et al.*, "A micro racetrack optical resonator test structure to optimize pattern approximation in direct lithography technologies," in *Proc. IEEE 32nd Int. Conf. Microelectron. Test Struct. (ICMTS)*, Kita-Kyushu City, Japan, Mar. 2019, pp. 4–7, doi: 10.1109/ICMTS.2019.8730981.
[71] A. Higo *et al.*, "Experimental comparison of rapid large-area direct electron beam exposure methods with plasmonic devices," *Sensors Mater.*, vol. 31, no. 8, p. 2511, Aug. 2019, doi: 10.18494/SAM.2019.2443.
[72] Z. Li *et al.*, "Meta-optics achieves RGB-achromatic focusing for virtual reality," *Sci. Adv.*, vol. 7, no. 5, Jan. 2021, Art. no. eabe4458, doi: 10.1126/sciadv.abe4458.

Satoshi Ikezawa (Member, IEEE) was born in Saitama, Japan. He received the Doctorate degree from the Graduate School of Information, Production, and Systems, Waseda University, in 2009. He was employed by Waseda University as an Assistant Professor and then an Assistant Professor, and in 2017, he became an Associate Professor at Kyushu University. Since 2019, he has been an Assistant Professor with the Tokyo University of Agriculture and Technology, working on developing new metasurface optical devices and optical evaluation systems. His research interests include MEMS/NEMS, laser spectrometers, optical fiber sensing systems, environment measurement, and interfacial analysis. He is a member of LSJ, Laser Chaos Committee, JSAP, IEEJ, IMEKO (TC19), ICST Program Member, and IEEE International Workshop on Metrology for AeroSpace Program Member.

Ryota Yamada was born in Kanagawa, Japan. He received the B.S. degree in mechanical systems engineering from the Tokyo University of Agriculture and Technology in 2022. He is pursuing the master's degree, working on developing new metasurface optical devices and optical evaluation systems. He entered the Department of Mechanical Systems Engineering, Tokyo University of Agriculture and Technology, in 2018.

Kosuke Takaki was born in Kanagawa. He received the B.S. degree in mechanical systems engineering from the Tokyo University of Agriculture and Technology in 2021. Currently, he is a member of the Department of Mechanical Systems, Graduate School of Engineering, Tokyo University of Agriculture and Technology. He is also a member of IEEJ.

Chikara Ogawa received the B.S. degree in mechanical systems engineering and the M.S. degree in industrial technology and innovation from the Tokyo University of Agriculture and Technology in 2020 and 2022, respectively.

Kentaro Iwami (Member, IEEE) was born in Miyagi, Japan. He received the Graduate degree from the Department of Mechatronics and Precision Engineering, School of Engineering, Tohoku University, in 2003, and the Doctorate degree from the Department of Nanomechanics, Graduate School of Engineering, in 2008. He became a JSPS Research Fellow (DC1) in 2005, an Assistant Professor at the Department Mechanical Systems Engineering, Graduate School of Engineering, Tokyo University of Agriculture and Technology, in 2008, and a Visiting Scholar at Stanford University in 2011. Since 2012, he has been an Associate Professor at the Graduate School of Engineering, Tokyo University of Agriculture and Technology. His research interest is NEMS/MEMS using metasurface plasmonics. He is a member of JSME, JSAP, IEEJ, OSJ, and ACS.